Energy Reports 6 (2020) 445–454

Contents lists available at ScienceDirect

Energy Reports

journal homepage: www.elsevier.com/locate/egyr

Research paper

Exergy analysis of solar desalination systems based on passive multi-effect membrane distillation

Francesco Signorato [a,1], Matteo Morciano [a,b,1], Luca Bergamasco [a], Matteo Fasano [a], Pietro Asinari [a,b,*]

[a] Department of Energy, Politecnico di Torino, Corso Duca degli Abruzzi 24, 10129 Torino, Italy
[b] Clean Water Center, Politecnico di Torino, Corso Duca degli Abruzzi 24, 10129 Torino, Italy

ARTICLE INFO

Article history:
Received 28 November 2019
Received in revised form 28 January 2020
Accepted 12 February 2020
Available online xxxx

Keywords:
Sustainability
Exergy analysis
Water treatment
Membrane distillation
Solar energy

ABSTRACT

Improving the efficiency and sustainability of water treatment technologies is crucial to reduce energy consumption and environmental pollution. Solar-driven devices have the potential to supply off-grid areas with freshwater through a sustainable approach. Passive desalination driven by solar thermal energy has the additional advantage to require only inexpensive materials and easily maintainable components. The bottleneck to the widespread diffusion of such solar passive desalination technologies is their lower productivity with respect to active ones. A completely passive, multi-effect membrane distillation device with an efficient use of solar energy and thus a remarkable enhancement in distillate productivity has been recently proposed. The improved performance of this distillation device comes from the efficient exploitation of low-temperature thermal energy to drive multiple distillation processes. In this work, we analyze the proposed distillation technology by a more in-depth thermodynamic detail, considering a Second Law analysis. We then report a detailed exergy analysis, which allows to get insights on the production of irreversibilities in each component of the assembly. These calculations provide guidelines for the possible optimization of the device, since simple changes in the original configuration may easily yield up to a 46% increase in the Second Law efficiency.

1. Introduction

Equitable access to clean water and sanitation services is a Human Right, as explicitly recognized by the General Assembly of the United Nations in 2010 (UN General Assembly, 2010). Nonetheless, today more than two billion people still live in regions suffering high water stress, while more than four billions experience severe water scarcity for at least one month during the year. Water scarcity is expected to be one of the major risks for society in the future, since the global water demand is steadily increasing at around 1% pace per year, prefiguring a nearly 30% increase by 2050 (UNESCO World Water Assessment Programme, 2019). The increase in water demand is mainly driven by population growth and industrial development, being the most water stressed areas located in developing countries and emerging economies (Vörösmarty et al., 2000; Elimelech and Phillip, 2011). In this sense, the development of simple, sustainable and affordable desalination technologies is a promising route to a more equitable access to clean water, which must overcome social and economic inequalities (Ahmed et al., 2019).

The well-established active desalination technologies are typically high-energy consuming, involve mechanical moving parts and are thus subject to risk of failure and frequent maintenance. Therefore, active desalination processes are best-suited for large installations, since they involve considerable installation and operating costs (Cipollina et al., 2009; Calise et al., 2016; Baccioli et al., 2018; Rosales-Asensio et al., 2019; Ghaffour et al., 2019). Instead, passive desalination technologies do not involve any moving part or electromechanical auxiliary system, being thus robust and implementable following a simple, compact and low-cost rationale (Arunkumar et al., 2019; Boriskina et al., 2019). Such passive technologies are thus promising candidates to help alleviating clean water scarcity in remote and impoverished regions of the world (Dongare et al., 2017; Morciano et al., 2017; Wang, 2018), where only salty or contaminated water and off-grid energy from generator sets or renewable sources (Boamah and Rothfuß, 2018; Bocca et al., 2018; Alberghini et al., 2019; Falchetta et al., 2019; Chen et al., 2016; Morciano et al., 2016) are available. The limit to a widespread diffusion of these technologies is currently their distillate productivity, which is generally lower than that of the active ones (Subramani and Jacangelo, 2015; Ni et al., 2018; Ahsan et al., 2012).

* Corresponding author at: Department of Energy, Politecnico di Torino, Corso Duca degli Abruzzi 24, 10129 Torino, Italy.
E-mail address: pietro.asinari@polito.it (P. Asinari).

[1] Equal contributors.

https://doi.org/10.1016/j.egyr.2020.02.005

A simple and low-cost membrane distillation device has been recently proposed by some of the present authors in a previous work (Chiavazzo et al., 2018). The concept relies on multiple distillation stages arranged in cascade, which yield an efficient energy management and thus larger distillate productivity with respect to previous systems in the literature. The required low-grade thermal power can be provided e.g. by solar energy, which is used to drive multiple distillation processes before it is lost to the environment. Distillation is carried out through a series of evaporation and condensation stages made of hydrophilic wicks, which are separated from each other by hydrophobic membranes. The treated saltwater is supplied to the system thanks to the capillary properties of the wicks, thus making the device completely passive, robust and suitable for operation in off-grid conditions. A detailed analysis of the energy management in the proposed distiller along with a developed theoretical model are discussed in the aforementioned article (Chiavazzo et al., 2018).

In this work, the proposed passive, multi-effect, membrane distillation device is analyzed with a more in-depth thermodynamic detail, thanks to a Second Law analysis. We then proceed with an exergetic analysis (Bejan, 2016; Dincer and Cengel, 2001; Mistry and Lienhard, 2013; Mohammadi et al., 2018), which allows to gain insight on the production of irreversibilities in each component of the assembled device. In detail, the exergy associated with the inlet solar irradiance, as well as the flow and non-flow exergy of salt and distilled water are defined and computed for the tested device, considering both chemical and thermomechanical contributions. The exergetic efficiency of the considered distiller is then compared to other solutions proposed in the literature. The reported analysis eventually allows to identify the main sources of entropy generation (or, equivalently, exergy destruction), and thus to suggest proper guidelines for a further optimization of the device. Some considerations on the possible optimization of distillate productivity are finally discussed on the basis of the validated physical model of the distillation device. Despite exergetic analysis has been already carried out for similar devices — e.g. solar stills (Torchia-Nunez et al., 2008; Tiwari et al., 2009; Ranjan and Kaushik, 2013; Mistry et al., 2011), to the best of the authors' knowledge it has never been applied to a multi-stage passive device.

The article is organized as follows. In Section 2 we introduce the thermodynamic framework underlying this work, namely the exergetic analysis of desalination systems. The results along with a discussion on the exergy destruction and cost of each component of the assembled device are reported in Section 3. Moreover, improvements to the original implementation of the distillation device are presented and the resulting Second Law efficiency compared with that of other desalination technologies. Finally, the conclusions are drawn in Section 4, and perspectives of the present work discussed.

2. Thermodynamics of desalination

2.1. General framework for exergy analysis

Exergy is the maximum amount of useful work that can be obtained from a reversible process through which a given system reaches equilibrium with a specifically-defined environment, starting from an initial state. The exergy equation for an open system can be obtained from the First and Second Law as (Lienhard et al., 2017)

$$\sum_{j=1}^{M} \Psi_j - W_t = \frac{d}{dt}\left(C + E_k + E_p\right)_{CV} + + \sum_{i=1}^{N} G_i\left(\zeta + e_k + e_p\right)_i + T_0\,\Sigma_{irr}. \tag{1}$$

In the above equation, $\Psi_j = Q_j\theta_j$ is the generic thermal exergy flux, with Q_j being thermal power and $\theta_j = 1 - T_0/T_j$ the *Carnot factor*; W_t the mechanical power; $C = U + p_0V - T_0S$, with U the internal energy, p_0 and T_0 the environment (*dead state*) pressure and temperature, V the total volume of the system enclosed in an arbitrary control volume (CV) and S the entropy. E_k and E_p represent the kinetic and potential energy, respectively. The mass flow rate is G_i, and $\zeta = h - T_0s$, being h and s the mass specific enthalpy and entropy, e_k and e_p are the specific counterparts of kinetic and potential energy, respectively. The last term on the right-hand side, $T_0\,\Sigma_{irr} = \Psi_{irr} \geq 0$, accounts for the exergy destruction within the system. If t superscript is adopted to indicate total quantities (*i.e.* including kinetic and potential energies), the above equation can be rewritten in a more compact form as

$$\sum_{j=1}^{M} \Psi_j - W_t = \frac{d}{dt}\left(A^t\right)_{CV} + + \sum_{i=1}^{N} G_i b_i^t + \sum_{i=1}^{N} G_i(\zeta_0)_i + \Psi_{irr}, \tag{2}$$

being A^t the non-flow total exergy related to the storage in the system, which is defined with respect to a reference state as $A^t = C^t - C_0$, and b_i^t the total specific flow exergy, defined as $b_i^t = \zeta^t - \zeta_0$.

2.2. Insight on multi-component systems

In case of multi-component systems, the effect related to the different composition of chemical species is typically made explicit. Let us consider a system containing a mixture of different species (for the non-flow exergy A^t) and the related mass flow rates (for the flow exergy b^t). Defining the specific Gibbs free energy as $g = u + pv - Ts$, the specific non-flow exergy ($a = A/m$, being m the total mass of the system) can be written as

$$\begin{aligned} a &= (u - u_0) + p_0\,(v - v_0) - T_0\,(s - s_0) = \\ &= \left(u - u^*\right) + p_0\left(v - v^*\right) - T_0\left(s - s^*\right) + \\ &+ \left(u^* - u_0\right) + p_0\left(v^* - v_0\right) - T_0\left(s^* - s_0\right) = \\ &= \left(u - u^*\right) + p_0\left(v - v^*\right) - T_0\left(s - s^*\right) + \left(g^* - g_0\right), \end{aligned} \tag{3}$$

where the starred notation represents the (intermediate) *restricted dead state* of the mixture system, which is characterized by the temperature T_0 and pressure p_0. In Eq. (3), the first three terms on the right-hand side represent the thermo-mechanical exergy, whilst the last term the chemical exergy. Similarly, the specific flow exergy yields

$$b = \left(h - h^*\right) - T_0\left(s - s^*\right) + \left(g^* - g_0\right). \tag{4}$$

Recalling that, in a mixture, $g = \sum \mu_k w_k/M_k$ (where $w_k = m_k/\sum_j m_j$ is the mass fraction, μ_k the chemical potential and M_k the molar mass of kth component), we obtain the general expressions for exergy in case of multi-component systems:

$$a = \left(u - u^*\right) + p_0\left(v - v^*\right) + - T_0\left(s - s^*\right) + \sum_k \left(\mu_k^* - \mu_k^0\right)\frac{w_k}{M_k}, \tag{5}$$

$$b = \left(h - h^*\right) - T_0\left(s - s^*\right) + \sum_k \left(\mu_k^* - \mu_k^0\right)\frac{w_k}{M_k}. \tag{6}$$

If the molar fraction of the kth component of a mixture is defined as

$$x_k = w_k\frac{M}{M_k} \tag{7}$$

with $M = \sum_k x_k M_k$, its chemical potential under the hypothesis of ideal solution can be computed as

$$\mu_k = \mu_{pure,k}(T, p) + RT \ln x_k, \tag{8}$$

where $\mu_{pure,k}$ is the chemical potential of the pure species and R the gas constant. Hence, the chemical component of exergy in Eqs. (5) and (6) can be re-written as

$$\sum_k \left(\mu_k^* - \mu_k^0\right) \frac{w_k}{M_k} = T_0 \sum_k R_k w_k \ln \frac{x_k}{x_k^0}, \tag{9}$$

being $R_k = R/M_k$ and x_k^0 the molar fraction of the kth component at dead state.

3. Results and discussion

3.1. Analysis of the device

A schematics of the considered passive multi-effect membrane distillation device is shown in Fig. 1. The device relies on multiple distillation stages, each of which consists of an aluminum sheet, a hydrophilic porous wick which acts as evaporator, a hydrophobic membrane (or an air gap obtained with a plastic spacer), and a hydrophilic wick which acts as condenser. Salt water is fed to each evaporator by capillary forces through some hydrophilic strips immersed in a salt water basin; whereas, freshwater is discharged to a freshwater basin by gravity through a strip protruding from the porous wick. Solar (thermal) energy generates a temperature gradient across the evaporators and the condensers, which is the driving force of the whole distillation process. In fact, such temperature difference causes a vapor pressure difference between each evaporator and condenser, which allows to overcome the one due to the salinity (*i.e.* activity) difference between the two wicks. As a result, the vapor pressure is higher on the salt water side, therefore causing a net water vapor flux from the evaporating to the condensing wicks through the membrane (or air gap). The hydrophobic membrane or the air gap are designed to allow the transport of the vapor phase only, while separating the liquid ones. The first evaporation is driven by the absorbed solar thermal energy; whereas, the distillation process in the successive evaporators is powered by the enthalpy of condensation released from the condenser above. The last-stage condenser eventually discharges the enthalpy of condensation into the environment through a heat sink. Notably, other sources of low-temperature heat, e.g. from the cooling system for internal combustion engine (Morciano et al., 2020), could be employed to drive the distillation process. An extensive analysis and discussion of the device, which will be labeled as *Distiller 1 − D1* in the followings, can be found in Chiavazzo et al. (2018).

The analysis presented in the current work is based on the predictions obtained by the theoretical model experimentally validated in the previous article (Chiavazzo et al., 2018). The distillation device analyzed here consists of 1, 3 or 10 identical stages. In each stage, the two hydrophilic layers (evaporator and condenser) are separated by a hydrophobic microporous membrane (thickness $t = 150$ μm) (see Fig. 2a). The top side of the distiller is made of a spectrally selective solar absorber to convert solar radiation into heat (solar absorbance $\alpha = 0.96$; infrared emissivity $\epsilon = 0.04$), covered by a transparent convection reducer to limit heat losses (effective heat transfer coefficient $= 2.3$ W m^{-2} K^{-1} (Chiavazzo et al., 2018); optical transmittance $\tau = 0.86$). A heat sink (effective heat transfer coefficient $\approx$ 30 W m^{-2} K^{-1}) is coupled to the bottom side of the stack, to reject the heat flux to the environment. Assuming a solar irradiance of 900 W m^{-2}, the device can produce up to 3.28 L m^{-2} h^{-1} in case of the 10-stage configuration (quantities normalized by the solar absorbing surface $A_s = 1.44 \times 10^{-2}$ m^2).

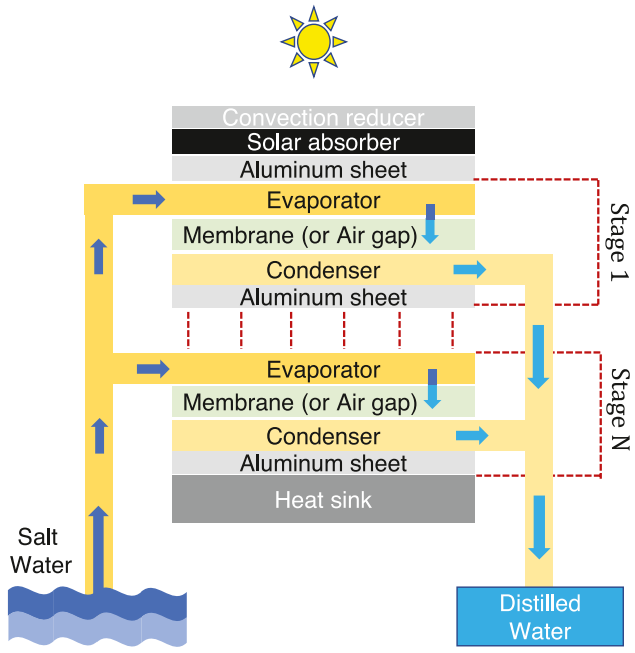

Fig. 1. Schematics of the multi-stage concept of the analyzed distillation device. Each stage consists of an aluminum sheet, a hydrophilic wick which acts as an evaporator, a hydrophobic membrane (or air gap obtained with a spacer), and a hydrophilic wick which acts as a condenser. Salt water is provided to the evaporators by capillary action, while freshwater is released by gravity through the porous wick. The whole distillation process is empowered by the solar (thermal) energy absorbed on the top surface of the device.

The overall control volume CV(a) of the device is chosen to ensure that all the outgoing heat fluxes flow into the environment (see Fig. 2a). Hence, the only useful effect of the device is the chemical one, namely the water distillation. The dead state is characterized by ambient temperature ($T_0 = 293.15$ K) and pressure ($p_0 = 101325$ Pa) and by a NaCl concentration in solution equal to the one of seawater, namely 35 g L^{-1} (*i.e.* $x^0_{NaCl} = x_0 = 0.021$). The thermodynamic properties are computed according to Nayar et al. (2016) and Sharqawy et al. (2010). In detail, the enthalpy and entropy of seawater at the dead state are equal to $h_0 = 79.8$ kJ kg^{-1} and $s_0 = 0.282$ kJ kg^{-1} K^{-1}, respectively. First, Eq. (2) is applied to the control volume CV(a) in Fig. 2, and this yields

$$\Psi_{irr} = \Psi_{Sun} + G_{in} b^t_{in} - G_{out} b^t_{out} + (G_{in} - G_{out})\zeta_0 - \frac{d}{dt}\left(A^t\right)_{CV_{(a)}}. \tag{10}$$

Different approaches to evaluate the maximum work that can be extracted from solar energy (exergy budget, Ψ_{Sun}) have been proposed in the literature (Bejan, 2016). In this work we adopt the expression proposed by Petela (1964)

$$\Psi_{Sun} = Q_{solar}\theta_p = Q_{solar}\left(1 - \frac{4}{3}\frac{T_0}{T_{Sun}} + \frac{1}{3}\frac{T_0^4}{T_{Sun}^4}\right), \tag{11}$$

with Q_{solar} being the energy flux from the Sun and $T_{Sun} = 6000$ K. It is worth to point out that the exergy content related to the radiative heat flux (Q_{rad}), the convective heat fluxes ($Q_{conv,top}$, $Q_{out,sink}$) and the optical losses ($(1 - \alpha\tau)Q_{solar}$) vanish, because they all flow into the ambient at dead state conditions (*i.e.* null Carnot factor). Moreover, the input and output temperatures of the salt and distilled water are equal to the environment one, thus the enthalpy and entropy contributions vanish too. Hence, considering an ideal binary mixture made of NaCl (molar fraction: x) and water (molar fraction: $(1 - x)$), Eqs. (6) and (9) can be

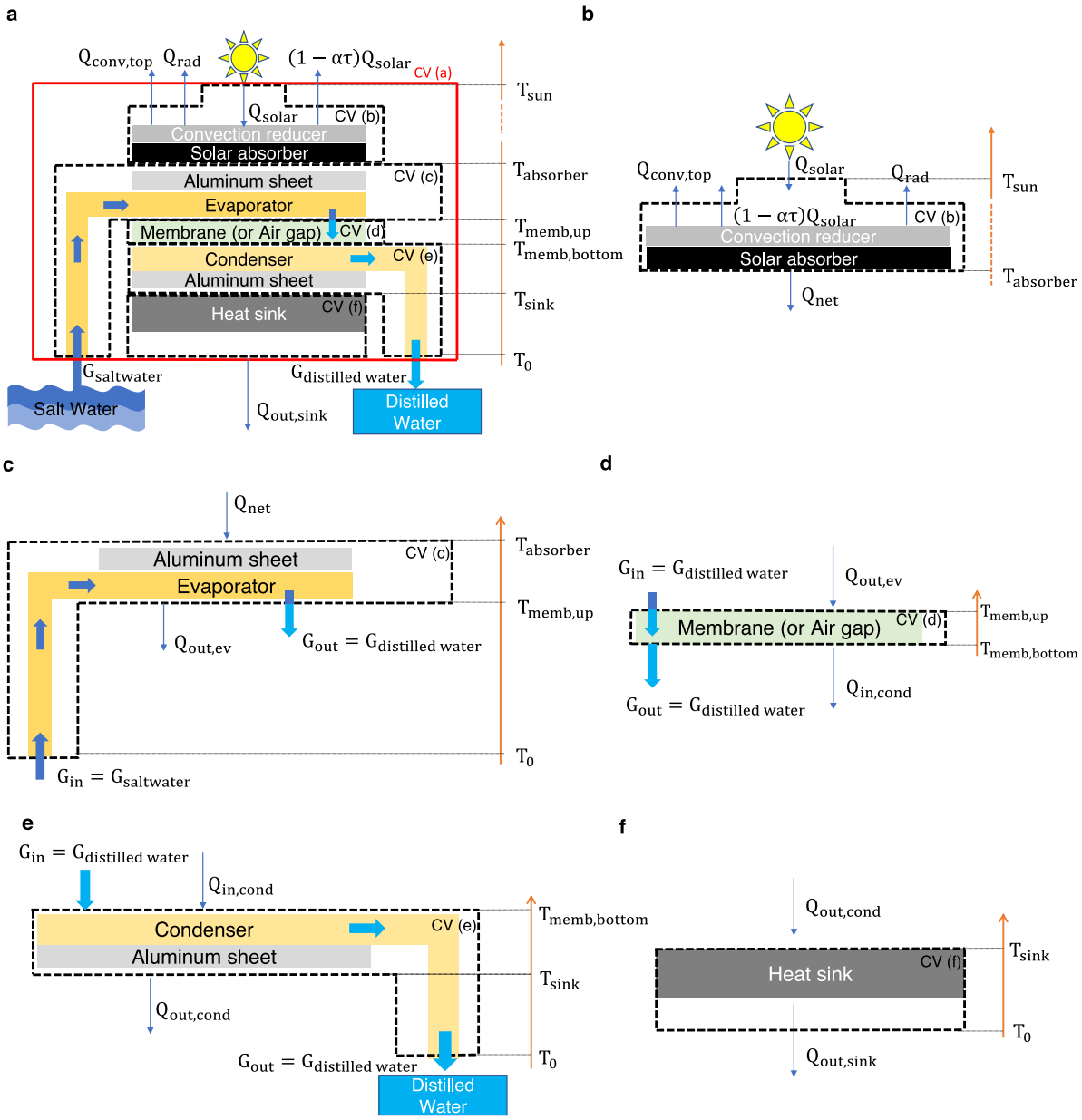

Fig. 2. Control Volumes (CV) used for the exergy analysis of the passive distillation device. (**a**) Control volume CV(a) (red solid line) used for the exergy analysis of the overall device. The useful effect is the variation of the chemical flow exergy (*i.e.* from salt to distilled water), which is driven by the input solar flux ($q_{solar} = Q_{solar}/A_s = 900$ W m^{-2}, being $A_s = 1.44 \times 10^{-2}$ m^2 the solar absorbing surface). The sub-systems are delimited by black dashed lines. For illustrative purposes, a 1-stage device is depicted here. (**b**) CV(b) includes the convection reducer and the spectrally selective absorber. (**c**) CV(c) includes the aluminum plate and the evaporator. In this CV, the saltwater flow rate G_{in} is heated up to temperature $T_{memb,up}$ and then vaporizes, thanks to the net heat flux Q_{net} transferred through the absorber. (**d**) CV(d) encloses the hydrophobic membrane (or the air gap), which is crossed by the vapor mass flow rate. (**e**) CV(e) includes the condenser and the aluminum plate. Here the vapor mass flow rate G_{in} is condensed and then discharged into the basin of distilled water. (**f**) CV(f) includes the heat sink, through which heat flux is released to the environment by convection. The orange vertical axes show the temperatures through the device.

re-called to write Eq. (10) as

$$\Psi_{irr} = \Psi_{Sun} + G_{in}\, R_w T_0 \left[x_{in} \ln\left(\frac{x_{in}}{x_0}\right) + (1 - x_{in}) \ln\left(\frac{1 - x_{in}}{1 - x_0}\right)\right] + - G_{out}\, R_w T_0 \left[x_{out} \ln\left(\frac{x_{out}}{x_0}\right) + (1 - x_{out}) \ln\left(\frac{1 - x_{out}}{1 - x_0}\right)\right] + + (G_{in} - G_{out})\zeta_0 - \frac{d}{dt}\left(A^t\right)_{CV_{(a)}}, \quad (12)$$

where $R_w = R/M_w$ is the specific gas constant of water vapor, since $x \ll 1$ and thus $M \approx M_w$. Considering CV(a), the inlet and outlet molar fractions of NaCl in the solution are $x_{in} = x_0$ (seawater) and $x_{out} = 0$ (distilled water), respectively; therefore, Eq. (12) can be re-written as

$$\Psi_{irr} = \Psi_{Sun} - G_{out}\, R_w T_0 \ln\left(\frac{1}{1 - x_0}\right) + + (G_{in} - G_{out})\zeta_0 - \frac{d}{dt}\left(A^t\right)_{CV_{(a)}}. \quad (13)$$

In Eq. (13), $(G_{in} - G_{out})\zeta_0$ can be safely neglected as it is one order of magnitude lower than the useful effect; whereas, $\frac{d}{dt}\left(A^t\right)_{CV_{(a)}}$ is – in principle – not negligible, since the salt progressively accumulates in the hydrophilic layers acting as evaporators during the

distillation process. Then, Eq. (13) simplifies to

$$\Psi_{irr} = \Psi_{Sun} - G_{out}\, R_w T_0 \ln\left(\frac{1}{1-x_0}\right) - \frac{d}{dt}\left(A^t\right)_{CV_{(a)}}. \tag{14}$$

In this case, the Second Law efficiency of the overall device can be finally defined as

$$\eta_{II} = \frac{G_{out}\, b^t_{out}}{\Psi_{Sun}} = 1 - \frac{\frac{d}{dt}\left(A^t\right)_{CV_{(a)}} + \Psi_{irr}}{\Psi_{Sun}}, \tag{15}$$

being Ψ_{Sun} computed through Eq. (11).

The results obtained for three different configurations of the distiller presented in Chiavazzo et al. (2018), namely the 1-, 3- and 10-stage device, are reported in Table 1. There, mass flow rate (G, L m^{-2} h^{-1}), irreversibility (Ψ_{irr}, W m^{-2}) and exergy storage term ($\frac{d}{dt}\left(A^t\right)_{CV(a)}$, W m^{-2}) are all normalized by the solar absorbing surface A_s, which is also equal to the evaporating surface. The gained output ratio (GOR), has been computed according to Gude (2018). The analysis is carried out considering the first 60 minutes of operations, when distillate productivity is not significantly affected by the salt accumulation in the evaporators (see some experimental evidences of this in the Supplementary Material of Chiavazzo et al. (2018)). The mass balance equation has been exploited to quantify the salt accumulated in each hydrophilic layer acting as evaporator during the test, that is

$$m_{NaCl} = m_{NaCl,t=0} + (G_{in} - G_{out})\,\Delta t, \tag{16}$$

being G_{in} and G_{out} constant with time as a first approximation. As a result, the molar fraction can be computed as:

$$x \cong \frac{m_{NaCl}/M_{NaCl}}{m_w/M_w}. \tag{17}$$

Eq. (17) assumes a fixed mass of water in the hydrophilic evaporators (m_w), which is estimated from the porosity and volume of the hydrophilic layers considered constant with time.

This exergy analysis allows then to identify the most relevant characteristics of the device that influence its distilled water productivity. As an illustrative example, a possible optimization of the stratigraphy of the multi-stage distiller has been investigated as well. In such a second version of the device, which will be labeled as *Distiller 2 — D2* in the followings, the hydrophobic membrane has been substituted by an air gap obtained through a plastic spacer (thickness ≈ 1.65 mm; porosity = 0.74). Furthermore, the convection reducer has been removed to reduce the costs (effective heat transfer coefficient = 5 W m^{-2} K^{-1}), and a more efficient heat sink considered (effective heat transfer coefficient = 156 W m^{-2} K^{-1}). The results obtained for three different device configurations, namely 1-, 3- and 10-stage device, are reported in Table 1: the improved distiller (D2) shows a relative enhancement in η_{II} of 40% (1 stage), 46% (3 stages) and 44% (10 stages) with respect to the original one (D1).

In Figs. 3 and 4 the salt concentration, exergy storage and destruction terms are shown as a function of time for the original (Chiavazzo et al., 2018) and optimized version of the device, respectively. In case of multi-stage configurations, the salt concentration is computed by averaging the values in all the n stages. Results show that the average salt concentration in the evaporators increases linearly with time in all the considered configurations. Note that, for the original version of the distiller (see Fig. 3a), the increase in salt concentration in the 1-stage configuration is higher than the multi-stage ones, because of the lower specific mass flow rate of distilled water per stage. As far as the improved version of the device is concerned (see Fig. 4a), the average mass flow rate of the 3-stage configuration is approximately equal to the one of a single stage device, thus the salt concentration transients are overlapped. Moreover, the higher total distilled mass flow rate in the 10-stage configuration leads to higher values of exergy storage. Finally, the sum of exergy storage and destruction results to be constant with time, because of the constant input solar flux and steady distilled mass flow rate considered during the transient. In particular, the latter approximation is justified by the experimental evidences reported in the Supplementary Material of Chiavazzo et al. (2018), where the expected decrease in distillate productivity due to the increased salinity in the evaporators cannot be appreciated up to the sensitivity of the used sensors during the first 60 min. Clearly, this effect cannot be neglected for longer time periods and, thus, the reported η_{II} are expected to reduce with time.

3.2. Analysis of each component of the device

A more detailed exergy analysis is necessary to understand how the various components of the distiller differently contribute to the overall irreversibility generation: the control volume CV(a) is therefore split into five control volumes (see Fig. 2), such that CV(a) = CV(b) ∪ CV(c) ∪ CV(d) ∪ CV(e) ∪ CV(f). The analysis has been carried out only for the 1-stage configuration, but it could be easily extended to the other cases.

The first control volume CV(b) (see Fig. 2b) includes the heat transfer from the sun to the solar absorber, and from the latter to the environment and evaporator. The bottom boundary is placed on the back side of the absorber, where the temperature is $T = T_{absorber}$. It is worth to point out that, in this case, the convective and radiative fluxes as well as the optical losses are considered at ambient temperature. The energy and exergy balances therefore simplify to

$$Q_{net} = Q_{solar} - (1-\alpha\tau)Q_{solar} - Q_{conv,top} - Q_{rad} \tag{18}$$

and

$$\Psi_{irr,1} = \Psi_{Sun} - Q_{net}\left(1 - \frac{T_0}{T_{absorber}}\right), \tag{19}$$

respectively.

The second control volume CV(c) (see Fig. 2c) includes the hydrophilic layer used as evaporator and the aluminum plate. The boundary through which salt water enters the control volume is placed at the seawater level; whilst, the output boundary is the interface between the evaporator and the hydrophobic membrane, meaning that the thermodynamic properties of the fluid are computed at $T = T_{memb,up}$. The variation of kinetic and potential energy through the control volume turns out to be negligible with respect to the other terms, since the speed of inlet/outlet fluid flow is of the order of mm s^{-1} and the maximum elevation of 5 cm (Chiavazzo et al., 2018). The exergy equation can be then written as

$$\begin{aligned}\Psi_{irr,2} = {} & Q_{net}\left(1 - \frac{T_0}{T_{absorber}}\right) - Q_{out,ev}\left(1 - \frac{T_0}{T_{memb,up}}\right) + \\ & - \frac{d}{dt}\left(A^t\right)_{CV_{(c)}} + (G_{in} - G_{out})\zeta_0 + \\ & - G_{out}\left[h_{out,ev} - h^* - T_0(s_{out,ev} - s^*)\right] + \\ & - G_{out}\, RT_0 \ln\left(\frac{1}{1-x_0}\right).\end{aligned} \tag{20}$$

Note that, the flow exergy associated with the inlet mass flow rate (G_{in}) vanishes because of the dead state conditions at the inlet boundary ($h_{in} = h^*$ and $s_{in} = s^*$). Moreover, as discussed earlier, $(G_{in} - G_{out})\zeta_0$ can be safely neglected.

The third control volume CV(d) (see Fig. 2d) encloses the hydrophobic membrane. The upper interface of the control volume coincides with the outlet section of CV(c), while the outlet one is chosen at the interface between the membrane and the

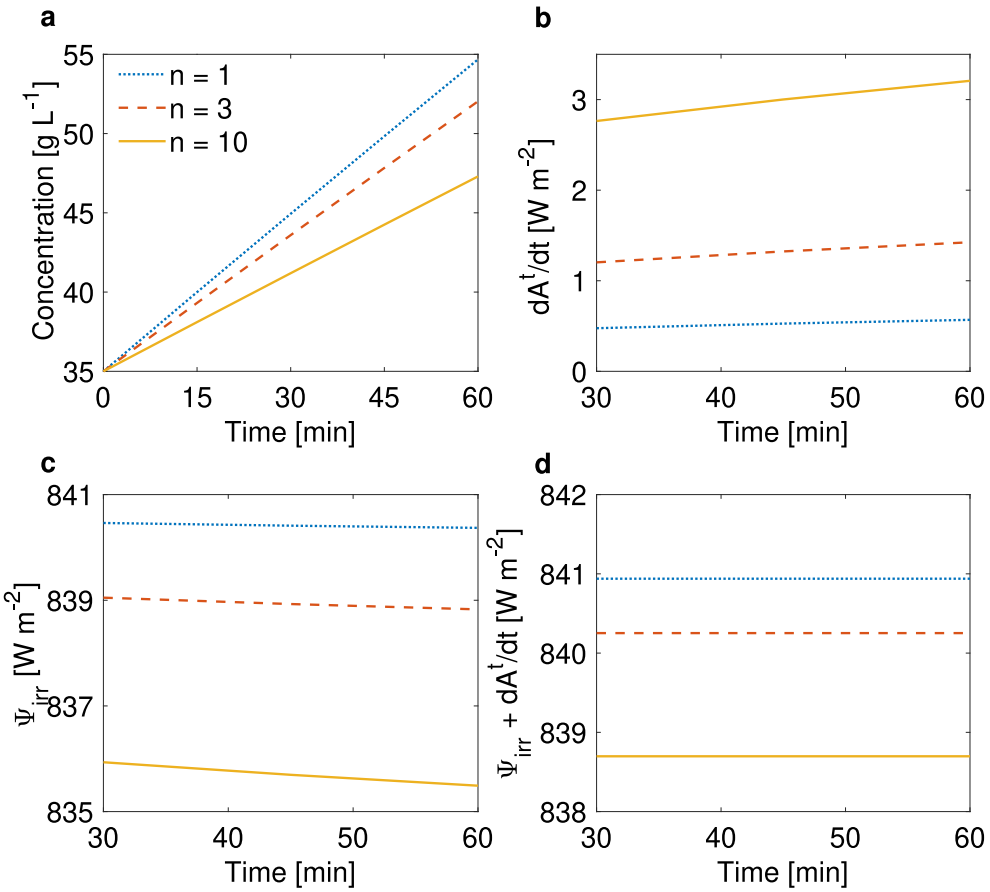

Fig. 3. Transient exergy analysis of the original version of the device (Chiavazzo et al., 2018) **for different number of distillation stages** (n). (**a**) Salt concentration of the solution in the evaporators, (**b**) exergy storage due to salt accumulation, **(c)** irreversibility production and (**d**) sum of the exergy storage and irreversibility production. In detail, three different configurations are considered: dotted blue, dashed red and yellow lines represent the 1-, 3- and 10-stage devices, respectively.

Table 1
Transient exergy analysis of the control volume CV(a), considering a different number n of distillation stages. The mass flow rates [L m^{-2} h^{-1}], the gained output ratio (GOR) [–] (Gude, 2018), the irreversibility and the storage terms [W m^{-2}], and the Second Law efficiency [%] are reported for D1 and D2, which refer to the original (Chiavazzo et al., 2018) and the improved version of the distiller, respectively.

n	G [L m^{-2} h^{-1}]		GOR [–]		Ψ_{irr} [W m^{-2}]		$\frac{d}{dt}\left(A^t\right)_{CV(a)}$ [W m^{-2}]		η_{II} [%]	
	D1	*D2*	*D1*	*D2*	*D1*	*D2*	*D1*	*D2*	*D1*	*D2*
1	0.53	0.68	0.37	0.47	840.37	840.05	0.57	0.77	0.05	0.07
3	1.37	1.45	0.95	1.01	838.83	837.45	1.42	2.29	0.13	0.19
10	3.28	4.78	2.29	3.34	835.49	832.25	3.21	5.21	0.32	0.46

hydrophilic layer acting as condenser. Here the heat flux is degraded from $T_{memb,up}$ to $T_{memb,bottom}$, and the exergy equation can be written as

$$\Psi_{irr,3} = Q_{out,ev}\left(1-\frac{T_0}{T_{memb,up}}\right) - Q_{in,cond}\left(1-\frac{T_0}{T_{memb,bottom}}\right) + \\ + G\left[h_{in,memb} - h_{out,memb} - T_0(s_{in,memb} - s_{out,memb})\right]. \quad (21)$$

Note that, $G_{in} = G_{out} = G_{distilled\ water} = G$.

The fourth control volume CV(e) (see Fig. 2e) takes into account the hydrophilic layer (condenser) supported by the aluminum plate, and the following exergy equation can be written:

$$\Psi_{irr,4} = Q_{in,cond}\left(1-\frac{T_0}{T_{memb,bottom}}\right) - Q_{out,cond}\left(1-\frac{T_0}{T_{sink}}\right) + \\ + G\left[h_{in,cond} - h_{out} - T_0(s_{in,cond} - s_{out})\right]. \quad (22)$$

Finally, the fifth control volume CV(f) (see Fig. 2f) includes the heat sink. Here the whole inlet exergetic flux is degraded to the ambient temperature, namely

$$\Psi_{irr,5} = Q_{out,cond}\left(1-\frac{T_0}{T_{sink}}\right). \quad (23)$$

Table 2
Temperature profile through the 1-stage distiller. Temperatures are given in K. D1 and D2 refer to the original (Chiavazzo et al., 2018) and the improved version of the distiller, respectively.

Temperature [K]	*D1*	*D2*
T_{sun}	6000	6000
$T_{absorber}$	320.3	310.1
$T_{memb,up}$	318.3	308.5
$T_{memb,bottom}$	317.4	299.6
T_{sink}	315.3	298.1
T_0	293.2	293.2

The temperature profile through the two versions of the distiller, as obtained from the experimentally validated model (Chiavazzo et al., 2018), are reported in Table 2. Considering those

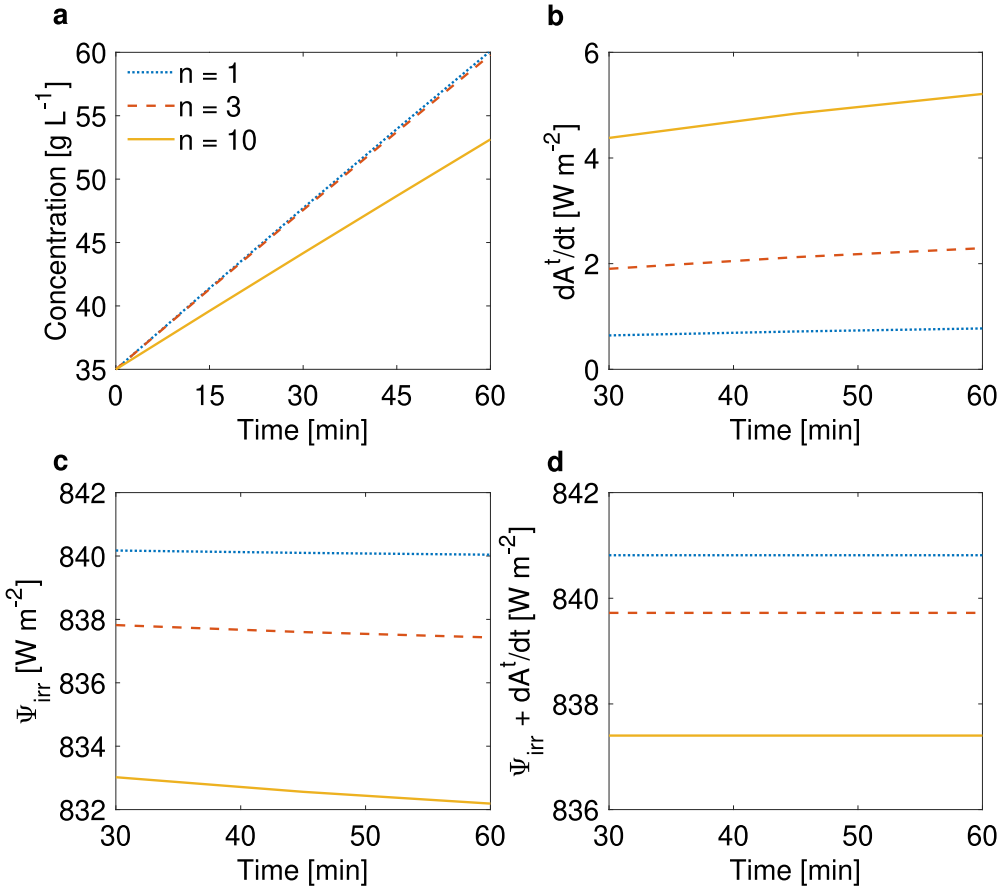

Fig. 4. Transient exergy analysis of the improved version of the device for different number of distillation stages (n). (**a**) Salt concentration of the solution in the evaporators, (**b**) exergy storage due to salt accumulation, (**c**) irreversibility production and (**d**) sum of the exergy storage and irreversibility production. In detail, three different configurations are considered: dotted blue, dashed red and yellow lines represent the 1-, 3- and 10-stage devices, respectively.

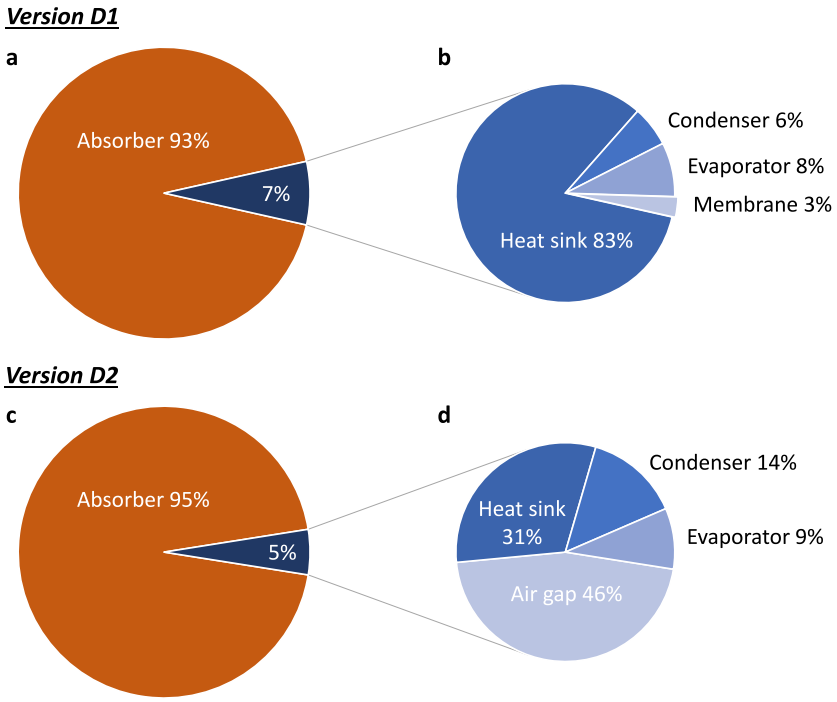

Fig. 5. Exergy analysis of the different components of a 1-stage passive distiller. Relative contribution to the irreversibility and exergy accumulation in the: (**a**) original version of the distiller (D1), with (**b**) detail within the stratigraphy and heat sink; (**c**) optimized version of the distiller (D2), with (**d**) detail within the stratigraphy and heat sink. Note that $\frac{d}{dt}\left(A^t\right) \neq 0$ only in the evaporator.

Table 3
Exergy destruction and accumulation in the different components of the 1-stage distiller. The irreversibility and storage terms are given in W m^{-2}. D1 and D2 refer to the original (Chiavazzo et al., 2018) and the improved version of the distiller, respectively.

Control volume	Component	$\Psi_{irr} + \frac{d}{dt}(A^t)$ [W m^{-2}]	
		D1	*D2*
b	Absorber	784.9	799.5
c	Evaporator	4.3	3.9
d	Membrane/Air gap	1.6	18.9
e	Condenser	3.5	5.9
f	Heat sink	46.8	12.6

temperature values, the results of exergy analysis for the different components of the distillers are presented in Table 3 and Fig. 5. Table 3 shows that, for both versions of the distiller, the higher source of exergy destruction and storage is represented by the solar absorber. In detail, it accounts for 93% (original distiller) and 95% (improved distiller) with respect to the overall amount (see Figs. 5a,c). Figs. 5b and 5d show the detailed irreversibility production within the stratigraphy of the distiller and in its heat sink. As far as the original solution is concerned, the major contribution is provided by the heat sink, because of its lower thermal efficiency. On the other hand, in the improved version of the distiller, a nearly 73% reduction of the destroyed and accumulated exergy has been achieved by installing a more efficient heat sink. At the same time, the optimization of the stratigraphy, which allows an increase in the distillate productivity, has led to sensibly higher exergetic losses in the spacer, due to the larger temperature gradient along the air gap.

3.3. Comparison with other technologies

A comparison between the results obtained for the proposed desalination device and other technologies reported in the literature is shown in Fig. 6. In detail, a tubular solar still, an active liquid gap membrane distillation (LGMD) system driven by a solar heat source, an active direct contact membrane distillation (DCMD) unit powered by a generic non-solar heat source and the 10-stage configuration of the present distiller (both original and improved version) are considered in the analysis.

First, the considered solar still consists of a tubular cover, a transparent polyvinyl chloride lid at both ends of the cover and a semicircular black trough inside it (Ahsan et al., 2012). This device relies on inclined surfaces to collect the condensed water from the lower edge of the still. The estimated Second Law efficiency of this solar still is equal to 0.055%.

Second, the considered solar LGMD system relies on three components: a solar collector, a photovoltaic (PV) module and a LGMD module (Luo and Lior, 2016). The solar collector heats up the feed stream of the LGMD module, the PV module provides the electricity for a pump and the LGMD module produces the distillate. The latter consists in a liquid gap membrane distillation configuration, which is a variation of an air gap membrane distillation (AGMD), where the gap between the membrane and the condensing surface is filled with the distilled water. This allows to achieve a higher GOR (Gude, 2018; Swaminathan et al., 2016). According to the exergy analysis performed in Luo and Lior (2016), the main sources of exergy destruction include the solar collector (84.6%), the PV module (10.2%) and the MD module (3.1%). The Second Law efficiency for this system is equal to 0.072%, which is slightly higher than classic solar stills.

Third, as far as the DCMD unit is concerned (Lienhard et al., 2017), the largest source of entropy generation is represented by the membrane. Similarly to reverse osmosis, the water vapor diffusion through the pores of the membrane is responsible of large irreversibilities, due to both high diffusion resistance and heat conduction losses through the membrane (as only a thin membrane separates the cold and hot streams in the module). This process presents a Second Law efficiency of approximately 1%.

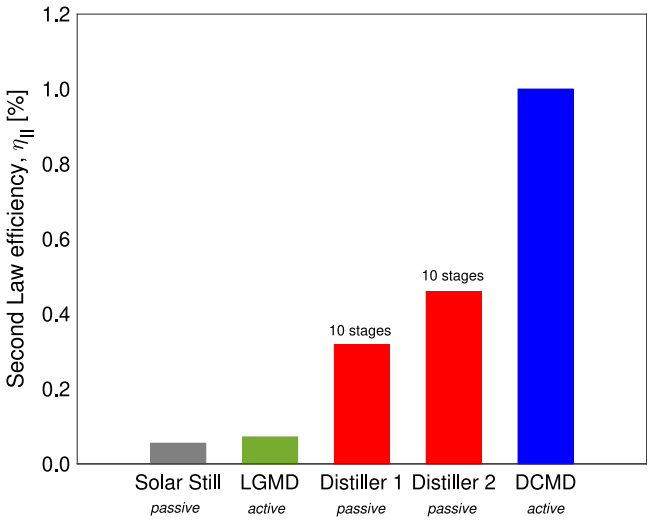

Fig. 6. Second Law efficiency for different desalination technologies. The Second Law efficiency for 10-stage configurations of the proposed device (both the original (Chiavazzo et al., 2018) and improved versions) presents intermediate values with respect to solar still (Ahsan et al., 2012), active liquid gap membrane distillation (LGMD) driven by solar source, and active direct contact membrane distillation (DCMD) powered by a generic non-solar heat source (Lienhard et al., 2017).

Fourth, the multi-stage distiller, because of its ability to reuse the latent heat of condensation, shows sensibly higher efficiency with respect to that of the solar still. The original version of the distiller shows a Second Law efficiency around 0.32%, whilst the improved version around 0.46% (namely, a 44% relative increase).

Note that, in all the previous cases, the efficiencies have been computed using the expression for solar exergy in Eq. (11). Moreover, efficiencies are evaluated considering the non-flow exergy (storage term) as part of the irreversibilities, as in Eq. (15). This means that, in this case, we consider that the high-salinity solution is not reused; however, the brine may be potentially reused and converted into a useful effect as well. For example, it may be exploited in other processes where high-salinity solutions are needed, such as forward osmosis processes, solar ponds or osmotic power generation (Linares et al., 2014; Martinetti et al., 2009; Ahmed et al., 2000; Lu et al., 2001; Ciofalo et al., 2019; Shaaban, 2019). In the latter case, the Second Law efficiency is envisioned to reach 1.08% in case of the 10-stage configuration device (improved version), which would be eventually comparable with the efficiency of active MD processes.

3.4. Cost analysis

An estimate of the costs of water production with the proposed devices is presented, based on the typical prices available on common online marketplaces for the required items. The analysis relies on the levelized cost of water (*LCOW*, here measured in terms of US dollars per liter of produced distillate). This latter index is defined as (Panchal et al., 2019; Kabeel et al., 2010)

$$LCOW = \frac{C_{cap}\, CRF + C_{op}}{G\, \Delta t_h}, \tag{24}$$

being C_{cap} the capital cost, *CRF* the capital recovery factor, C_{op} the operation and maintenance cost, G the productivity and Δt_h the

total operating hours (8 hours of solar desalination per day have been considered). The operation cost is estimated parametrically, as $C_{op} = C_{cap}\, CRF\, s\, n$, being s the considered share of the capital cost and n the considered number of years of useful lifetime. The capital recovery factor (CRF) is defined as:

$$CRF = i\,\frac{(1+i)^n}{(1+i)^n - 1}, \tag{25}$$

being i the interest rate. Here we assume $s = 10\%$ and $i = 12\%$. In order to estimate the possible range of cost, we study two scenarios: a more conservative one, that is, a 3-stage configuration and 2 years lifetime ($n = 2$); an optimal one, based on 10-stage configuration device and 10 years lifetime ($n = 10$). A one-square-meter device is considered in both cases.

The capital cost for the distiller D1 is $C_{cap} \approx 458$ USD. In detail, the hydrophobic PTFE membrane accounts for 20% of the total cost, the aluminum sheets for 6%, the hydrophilic microfiber wicks for 3.5%, the selective solar absorber for 1.5%, the 3D printed convection reducer for 15% and the heat sink for 54%. Note that, for the sake of simplicity, the following contributions are neglected: polystyrene floating element, auxiliaries (namely hydraulic/mechanical fittings), distilled water basin and pumps for distillate/rinsing. Based on the more conservative scenario (namely 2 years lifetime and 3-stage configuration device), we obtain $LCOW \approx 0.04$ USD L^{-1}; whereas, in case of 10-stage configuration device and 10 years lifetime the levelized cost of water reduces to $LCOW \approx 0.0027$ USD L^{-1}.

In the improved version of the distiller D2, the 3D printed convection reducer is removed and the membrane is substituted with a plexiglass porous frame (spacer). Then, the list of materials includes the hydrophilic layers (fabrics), the heat sink, the plexiglass frame and the aluminum sheets for preventing contamination. The plexiglass accounts for 7.5% of the total cost, the aluminum sheets for 8.5%, the hydrophilic microfiber wicks for 4%, the selective solar absorber for 2% and the heat sink for 78%. The total cost of the analyzed device then yields $C_{cap} \approx 321$ USD. The estimated levelized cost of water is about $LCOW \approx 0.027$ USD L^{-1} for the more conservative and 0.0011 USD L^{-1} for the best considered scenarios, respectively. The cost reduction of the improved version of the distiller is then up to about 60%, in the best scenario, with respect to the original version.

4. Conclusions

Reducing energy consumption is key for minimizing the environmental footprint of desalination systems. In this sense, exergy analysis is a powerful technique to investigate the thermodynamic performance and sustainability of systems and processes (Lucia and Grisolia, 2019). In this work, we have applied this analysis to a previously proposed multi-stage distillation device, which is powered by solar energy and operates without the need of any moving part or electromechanical auxiliary system (*i.e.* passive desalination). The device provides enhanced freshwater productivity thanks to a smart recovery of the available low-grade thermal energy. The present exergetic analysis has allowed to have a more in-depth thermodynamic insight of the concept, with particular regards to the production of irreversibilities in each component of the device and the overall Second Law efficiency.

The results obtained show that the Second Law efficiency of the originally proposed device is higher than that reported for e.g. a tubular solar still. We have also shown that the exergy analysis allows to identify simple modifications of the distiller stratigraphy and assembly that may easily yield a further 40%–46% relative enhancement in the Second Law efficiency. These results demonstrate that the reported exergy analysis can be adopted for further optimization of the device and for an efficiency-driven re-design of those components of the stratigraphy that mainly impact the overall performance of the system.

The chemical exergy owned by the brine has been here considered as lost, therefore reducing the Second Law efficiency of the device. However, in perspective, the proposed distiller could be coupled with a desalination system operating with high-salinity feed water (e.g. forward osmosis), in order to reuse the brine and thus increase the overall performance of the desalination process. In this latter case, the obtained efficiency is envisioned to be comparable with that of e.g. direct contact membrane distillation devices, that is around 1%.

Declaration of competing interest

The authors declare that they have no known competing financial interests or personal relationships that could have appeared to influence the work reported in this paper.

CRediT authorship contribution statement

Francesco Signorato: Methodology, Formal analysis, Investigation, Data curation, Writing - original draft, Visualization. **Matteo Morciano:** Conceptualization, Validation, Formal analysis, Investigation, Writing - original draft, Visualization. **Luca Bergamasco:** Conceptualization, Formal analysis, Writing - review & editing. **Matteo Fasano:** Conceptualization, Formal analysis, Writing - review & editing. **Pietro Asinari:** Methodology, Supervision, Project administration, Funding acquisition.

Acknowledgments

The authors acknowledge Prof. Valter Giaretto for useful discussions. M.M. and P.A. acknowledge funding from the Clean Water Center at Politecnico di Torino.

References

Ahmed, F.E., Hashaikeh, R., Hilal, N., 2019. Solar powered desalination–technology, energy and future outlook. Desalination 453, 54–76.

Ahmed, M., Shayya, W.H., Hoey, D., Mahendran, A., Morris, R., Al-Handaly, J., 2000. Use of evaporation ponds for brine disposal in desalination plants. Desalination 130 (2), 155–168.

Ahsan, A., Imteaz, M., Rahman, A., Yusuf, B., Fukuhara, T., 2012. Design, fabrication and performance analysis of an improved solar still. Desalination 292, 105–112.

Alberghini, M., Morciano, M., Bergamasco, L., Fasano, M., Lavagna, L., Humbert, G., Sani, E., Pavese, M., Chiavazzo, E., Asinari, P., 2019. Coffee-based colloids for direct solar absorption. Sci. Rep. 9 (1), 4701.

Arunkumar, T., Ao, Y., Luo, Z., Zhang, L., Li, J., Denkenberger, D., Wang, J., 2019. Energy efficient materials for solar water distillation-a review. Renew. Sustain. Energy Rev. 115, 109409.

Baccioli, A., Antonelli, M., Desideri, U., Grossi, A., 2018. Thermodynamic and economic analysis of the integration of organic rankine cycle and multi-effect distillation in waste-heat recovery applications. Energy 161, 456–469.

Bejan, A., 2016. Advanced Engineering Thermodynamics, fourth ed. John Wiley & Sons Inc.

Boamah, F., Rothfuß, E., 2018. From technical innovations towards social practices and socio-technical transition? re-thinking the transition to decentralised solar pv electrification in africa. Energy Res. Soc. Sci. 42, 1–10.

Bocca, A., Bergamasco, L., Fasano, M., Bottaccioli, L., Chiavazzo, E., Macii, A., Asinari, P., 2018. Multiple-regression method for fast estimation of solar irradiation and photovoltaic energy potentials over europe and africa. Energies 11 (12), 3477.

Boriskina, S.V., Raza, A., Zhang, T., Wang, P., Zhou, L., Zhu, J., 2019. Nanomaterials for the water-energy nexus. MRS Bull. 44 (1), 59–66.

Calise, F., d'Accadia, M.D., Macaluso, A., Piacentino, A., Vanoli, L., 2016. Exergetic and exergoeconomic analysis of a novel hybrid solar–geothermal polygeneration system producing energy and water. Energy Conv. Manag. 115, 200–220.

Chen, Q., Li, Y., Chua, K., 2016. On the thermodynamic analysis of a novel low-grade heat driven desalination system. Energy Conv. Manag. 128, 145–159.
Chiavazzo, E., Morciano, M., Viglino, F., Fasano, M., Asinari, P., 2018. Passive solar high-yield seawater desalination by modular and low-cost distillation. Nature Sustain. 1 (12), 763.
Ciofalo, M., La Cerva, M., Di Liberto, M., Gurreri, L., Cipollina, A., Micale, G., 2019. Optimization of net power density in reverse electrodialysis. Energy 181, 576.
Cipollina, A., Micale, G., Rizzuti, L., 2009. Seawater Desalination, first ed. Springer-Verlag Berlin Heidelberg.
Dincer, I., Cengel, Y., 2001. Energy, entropy and exergy concepts and their roles in thermal engineering. Entropy 3 (3), 116–149.
Dongare, P.D., Alabastri, A., Pedersen, S., Zodrow, K.R., Hogan, N.J., Neumann, O., Wu, J., Wang, T., Deshmukh, A., Elimelech, M., et al., 2017. Nanophotonics-enabled solar membrane distillation for off-grid water purification. Proc. Natl. Acad. Sci. 114 (27), 6936–6941.
Elimelech, M., Phillip, W.A., 2011. The future of seawater desalination: energy, technology, and the environment. Science 333 (6043), 712–717.
Falchetta, G., Pachauri, S., Parkinson, S., Byers, E., 2019. A high-resolution gridded dataset to assess electrification in sub-saharan africa. Sci. Data 6 (1), 110.
Ghaffour, N., Soukane, S., Lee, J.-G., Kim, Y., Alpatova, A., 2019. Membrane distillation hybrids for water production and energy efficiency enhancement: A critical review. Appl. Energy 254, 113698.
Gude, V.G., 2018. Exergy evaluation of desalination processes. ChemEngineering 2 (2), 28.
Kabeel, A., Hamed, A., El-Agouz, S., 2010. Cost analysis of different solar still configurations. Energy 35 (7), 2901–2908.
Lienhard, J.H., Mistry, K.H., Sharqawy, M.H., Thiel, G.P., 2017. Chapter 4 Thermodynamics, Exergy, and Energy Efficiency in Desalination Systems. pp. 127–206.
Linares, R.V., Li, Z., Sarp, S., Bucs, S.S., Amy, G., Vrouwenvelder, J.S., 2014. Forward osmosis niches in seawater desalination and wastewater reuse. Water Res. 66, 122–139.
Lu, H., Walton, J.C., Swift, A.H., 2001. Desalination coupled with salinity-gradient solar ponds. Desalination 136 (1–3), 13–23.
Lucia, U., Grisolia, G., 2019. Exergy inefficiency: An indicator for sustainable development analysis. Energy Rep. 5, 62–69.
Luo, A., Lior, N., 2016. Critical review of membrane distillation performance criteria. Desalin. Water Treat. 57 (43), 20093–20140.
Martinetti, C.R., Childress, A.E., Cath, T.Y., 2009. High recovery of concentrated ro brines using forward osmosis and membrane distillation. J. Membrane Sci. 331 (1–2), 31–39.
Mistry, K., Lienhard, J., 2013. Generalized least energy of separation for desalination and other chemical separation processes. Entropy 15 (6), 2046–2080.
Mistry, K.H., McGovern, R.K., Thiel, G.P., Summers, E.K., Zubair, S.M., Lienhard, J.H., 2011. Entropy generation analysis of desalination technologies. Entropy 13 (10), 1829–1864.
Mohammadi, A., Ahmadi, M.H., Bidi, M., Ghazvini, M., Ming, T., 2018. Exergy and economic analyses of replacing feedwater heaters in a rankine cycle with parabolic trough collectors. Energy Rep. 4, 243–251.
Morciano, M., Fasano, M., Bergamasco, L., Albiero, A., Lo Curzio, M., Asinari, P., Chiavazzo, E., 2020. Sustainable freshwater production using passive membrane distillation and waste heat recovery from portable generator sets. Appl. Energy 258, 114086.
Morciano, M., Fasano, M., Salomov, U., Ventola, L., Chiavazzo, E., Asinari, P., 2017. Efficient steam generation by inexpensive narrow gap evaporation device for solar applications. Sci. Rep. 7 (1), 11970.
Morciano, M., Fasano, M., Secreto, M., Jamolov, U., Chiavazzo, E., Asinari, P., 2016. Installation of a concentrated solar power system for the thermal needs of buildings or industrial processes. Energy Procedia 101, 956–963.
Nayar, K.G., Sharqawy, M.H., Banchik, L.D., J. H. Lienhard, V., 2016. Thermophysical properties of seawater: a review and new correlations that include pressure dependence. Desalination 390, 1–24.
Ni, G., Zandavi, S.H., Javid, S.M., Boriskina, S.V., Cooper, T.A., Chen, G., 2018. A salt-rejecting floating solar still for low-cost desalination. Energy Environ. Sci. 11 (6), 1510–1519.
Panchal, H., Taamneh, Y., Sathyamurthy, R., Kabeel, A., El-Agouz, S., Naveen Kumar, P., Manokar, A.M., Arunkumar, T., Mageshbabu, D., Bharathwaaj, R., 2019. Economic and exergy investigation of triangular pyramid solar still integrated to inclined solar still with baffles. Int. J. Ambient Energy 40 (6), 571–576.
Petela, R., 1964. Exergy of heat radiation. J. Heat Transfer 86 (2), 187–192.
Ranjan, K., Kaushik, S., 2013. Energy, exergy and thermo-economic analysis of solar distillation systems: A review. Renew. Sustain. Energy Rev. 27, 709–723.
Rosales-Asensio, E., García-Moya, F.J., González-Martínez, A., Borge-Diez, D., de Simón-Martín, M., 2019. Stress mitigation of conventional water resources in water-scarce areas through the use of renewable energy powered desalination plants: An application to the canary islands. Energy Rep..
Shaaban, S., 2019. Performance optimization of an integrated solar combined cycle power plant equipped with a brine circulation msf desalination unit. Energy Convers. Manage. 198, 111794.
Sharqawy, M.H., Lienhard, J.H., Zubair, S.M., 2010. Thermophysical properties of seawater: a review of existing correlations and data. Desalinat. Water Treatment 16 (1–3), 354–380.
Subramani, A., Jacangelo, J.G., 2015. Emerging desalination technologies for water treatment: a critical review. Water Res. 75, 164–187.
Swaminathan, J., Chung, H.W., Warsinger, D.M., AlMarzooqi, F.A., Arafat, H.A., V, J.H.L., 2016. Energy efficiency of permeate gap and novel conductive gap membrane distillation. J. Membr. Sci. 502, 171–178.
Tiwari, G., Dimri, V., Chel, A., 2009. Parametric study of an active and passive solar distillation system: energy and exergy analysis. Desalination 242 (1–3), 1–18.
Torchia-Nunez, J., Porta-Gandara, M., Cervantes-de Gortari, J., 2008. Exergy analysis of a passive solar still. Renew. Energy 33 (4), 608–616.
UN General Assembly, 2010. Resolution a/res/64/292: The Human Right to Water and Sanitation.
UNESCO World Water Assessment Programme, 2019. The United Nations World Water Development Report 2019: Leaving No One behind. UNESCO, Paris.
Vörösmarty, C.J., Green, P., Salisbury, J., Lammers, R.B., 2000. Global water resources: vulnerability from climate change and population growth. Science 289 (5477), 284–288.
Wang, P., 2018. Emerging investigator series: the rise of nano-enabled photothermal materials for water evaporation and clean water production by sunlight. Environ. Sci. Nano 5 (5), 1078–1089.